PAPER

Check for updates

Rapid solid-state metathesis reactions for the formation of cobalt–iron monoboride solid-solutions and investigation of their water splitting electrocatalytic activity†

Janaka P. Abeysinghe [ID] and Edward G. Gillan [ID] *

Metal borides have received increased attention as potentially robust water splitting electrocatalysts. Some studies have reported synergistic electrocatalytic effects on hydrogen and/or oxygen evolution reactions (HER/OER) using mixed metal borides. This report describes the single-step, solvent-free, and rapid (few seconds) synthesis of a series of crystalline $Co_{1-x}Fe_xB$ ($x = 0-1$) solid solutions in high isolated product yields (>80%) from exothermic, self-propagating solid-state metathesis (SSM) reactions between metal halides and elemental Mg/B reactants. Powder X-ray diffraction shows the $Co_{1-x}Fe_xB$ products are single-phase with crystallite sizes near 60 nm. SEM/EDS and elemental analysis indicate products contain homogeneous Co/Fe distributions and form large micrometer-sized particle aggregates. The electrocatalytic HER with these well-structured crystalline $Co_{1-x}Fe_xB$ materials in 1 M KOH shows increased HER activity at lower applied potentials as cobalt content increases. The OER activity of $Co_{1-x}Fe_xB$ also generally shows improvement with increased cobalt content. Crystalline $Co_{1-x}Fe_xB$ catalysts exhibit good long-term 24 h HER and OER stability in 1 M KOH. Post-electrochemistry $Co_{1-x}Fe_xB$ analyses confirm the retention of product crystallinity after long term electrocatalysis.

Introduction

Providing sustainable energy alternatives to fossil fuels using renewable, low-cost, and environmentally friendly energy sources is a daunting challenge because global energy demand is expected to double or triple in the next few decades.[1,2] Hydrogen (H_2) is a major contender as a future fuel due to its high gravimetric energy density, renewable potential, and environmentally friendly use, and many countries have begun to examine hydrogen-fueled energy applications.[1,2] Several significant barriers exist for large-scale and sustained H_2 consumption including development of efficient, low-cost, and environmentally benign H_2 production methods and design

Department of Chemistry, University of Iowa, Iowa City, Iowa, 52242, USA.
E-mail: edward-gillan@uiowa.edu, janaka-abeysinghe@uiowa.edu

† Electronic supplementary information (ESI) available: Unit cell parameters of metal borides, 2θ (*d*-spacing) values of crystal planes, ICP and EDS Co/Fe ratios, EDS maps of metal borides before and after electrochemistry measurements, additional product SEM and TEM images, thermochemical reaction calculations and graphs for CoB, FeB and $Co_{0.5}Fe_{0.5}B$, mechanistic study results of SSM reactions, graphical and tabular results for electrocatalytic HER and OER studies, *iR* compensated HER and OER overlay graphs, chronoamperometric measurements, tables of literature comparison data, and XRD data on borides on C_{wax} tips after 24 hour electrocatalysis after HER and OER. See DOI: https://doi.org/10.1039/d3ma00728f

of gravimetrically useful H_2 storage containment. Three methods used for large scale H_2 production today are natural gas reforming, coal gasification, and water electrolysis. While water electrolysis only accounts for a few percent of global hydrogen production, it is potentially the most sustainable, lowest greenhouse gas emission H_2 production process. Water electrolysis ($H_2O \rightarrow H_2 + \frac{1}{2}O_2$) consists of two chemical reactions: the hydrogen evolution reaction (HER) and the oxygen evolution reaction (OER). A major issue with water electrolysis is that currently useful electrocatalysts for HER and OER are very expensive and rare (*e.g.*, Pt, Pd, IrO_2, and RuO_2). Extensive research is being conducted to identify robust electrocatalysts for water electrolysis that use more earth abundant and less expensive transition-metals, particularly those from the 3d series (*e.g.*, Cr to Cu).

Cobalt and iron compounds have been widely studied as HER and OER electrocatalysts. Some iron and/or cobalt transition metal phosphides,[3,4] oxide/hydroxides,[5,6] sulphides,[7,8] nitrides,[9,10] and borides[11,12] show moderate to good electrocatalytic activity for water electrolysis. Metal borides are an intriguing class of electrocatalyst materials because of their properties such as high electrical conductivity, thermal and corrosion resistance, high melting temperatures (>1000 °C), and chemical stability.[13–21] Several metal borides in crystalline

or amorphous structures (e.g., CoB_x,[22] NiB_x,[23] MoB_x,[24] VB_2,[25] WB_x[26]) have been studied as electrocatalysts for HER and/or OER. Some boride studies have focused on improving the electrocatalytic activity of metal borides via control of particle morphology (e.g., nanoparticles, nanosheets or amorphous structures), synthesis of more complex mixed metal borides and composites, and use of catalyst support (e.g., Ni mesh, carbon cloth).[27–31]

Metal borides can form a range of structures from metal-rich to boron-rich compositions that contain metal–metal interactions, boron–boron covalent bonds, and metal–boron bonds leading to diverse physical and chemical properties.[32] Typical metal boride syntheses either produce poorly crystalline products or require high temperature synthesis or post-reaction annealing to obtain crystalline products. Metal boride syntheses use traditional high-temperature elemental reactions and lower temperature precursor approaches, including arc melting,[33,34] reactive sintering,[35] solution-phase synthesis,[36–38] mechanochemical methods,[39] metal flux synthesis,[40,41] electrodeposition,[42] electroless deposition,[43] molten salt synthesis,[26,44] and hydrothermal reactions.[45] Several of these reactions use relatively inert elemental boron (mp $\sim$ 2000 °C) as a reactant in metal boride synthesis. A recent iodide exchange synthetic strategy with BI_3 and metal powders produced a range of metal-rich and boride-rich metal borides at moderate $\sim$600–800 °C temperatures.[46]

An alternative to externally heated materials synthesis that uses thermochemical energy provided by chosen reactants is known as solid-state metathesis (SSM).[47–50] Self-propagating SSM reactions can be initiated by brief reactant heating with a heated filament (ignition reaction) and the exothermic energy released is sufficient to initiate further reactions from surrounding reactants. SSM reactions are complete in a few seconds and usually yield polycrystalline micrometer-sized particle aggregates. The exothermicity of SSM reactions is often dictated by the formation of a stable byproduct salt (e.g., NaCl or $MgCl_2$) that becomes briefly molten during the reaction and can facilitate diffusion and crystallization.[48] Ignition SSM reactions have been used to synthesize a variety of transition metal compounds including metal phosphides,[51,52] nitrides,[53,54] oxides,[55,56] sulphides,[57] and few ternary mixed metal and non-metal compounds.[57–60] Typical SSM approaches to metal boride synthesis rely on either ignition or furnace initiated reactions between metal halides and MgB_2.[24,61] Our recent work showed that a rapid SSM strategy is successful with three mixed reactants [metal chloride, magnesium powder, and amorphous boron] to produce crystalline FeB, CoB, and NiB.[62] Several of these metal borides show moderate activity in HER and OER electrocatalysis.

Some recent studies have measured HER or OER electrocatalytic enhancements for mixed metal borides over their binary boride parent structures that are ascribed to synergistic effects from both metals being present on the boride surface. The mixed metal borides' increased catalytic activity has also been linked to the formation of specific morphologies[63,64] or favorable alterations in electronic structure or conductivity.[11,12,65] Co–Fe–B structures have been produced as crystalline or amorphous phases via liquid phase synthesis methods (chemical reduction, hydrothermal reactions, and molten-salt assisted borothermal reduction), but post-reaction calcination is often required to obtain crystalline metal borides.[11,12,63–67] Some prior studies used amorphous or poorly crystalline mixed-metal borides, making it difficult to clearly compare catalytic metal boride activities from different studies.

Since Co and Fe are two relatively earth-abundant metals, a clear comparison of well-structured Co–Fe–B solid-solution effects on HER and OER electrocatalysis is highly desirable. Our prior SSM work showed reaction success using mixed Mg/B reactants for metal boride synthesis.[62] In this study we describe the rapid SSM synthesis of a wide range of crystalline $Co_{1-x}Fe_xB$ solid solutions (x = 0–1) between mixtures of $FeCl_2/CoCl_2$ and Mg/B powders. This work demonstrates that a surprising level of atomic mixing is possible in rapid (few seconds) SSM reactions using four reactants with five different elements, to produce crystalline $Co_{1-x}Fe_xB$ and byproduct $MgCl_2$. Powder X-ray diffraction, SEM/EDS, XRF, and bulk elemental analysis support solid-solution formation with compositions that closely reflect the ratios of elements in the reaction mixture. The $Co_{1-x}Fe_xB$ materials were examined in HER and OER electrocatalysis in KOH electrolyte to identify trends in activity versus composition.

Experimental procedures

Starting materials and reagents

Anhydrous commercial reagents were stored in an inert atmosphere glove box and utilized as purchased: $CoCl_2$ (Alfa-Aesar, 99.7%), $FeCl_2$ (Aldrich Chemicals, 98%), Mg (Sigma-Aldrich, 99.5%, powder, −325 mesh), and amorphous B (Alfa-Aesar, 95–97%, powder (APS < 1 micron). 0.1 M HCl (Fisher Scientific, 12.4 M diluted with DI H_2O) was used for the product washing. ICP calibration standards were prepared by diluting Co (Thermo Fisher Scientific 999 $\pm$ 5 μg mL^{-1}), Fe (Thermo Fisher Scientific 1003 $\pm$ 6 μg mL^{-1}), B (Alfa Aesar 1000 μg mL^{-1}), Mg (Thermo Fisher Scientific 999 $\pm$ 5 μg mL^{-1}) in 5 vol% HNO_3 (from Sigma-Aldrich, 14 M and 18 MΩ ultra-pure water). Materials used for electrochemical studies: synthetic graphite powder (<20 μm, Sigma-Aldrich), paraffin wax (mp $\geq$ 65 °C, Sigma-Aldrich), 1.0 M KOH (Sigma-Aldrich, KOH pellets dissolved with 18 MΩ ultra-pure water), 10% Pt on Vulcan XC-72 carbon (C1-10 fuel cell grade, E-Tek), and RuO_2 (Alfa-Aesar, 99.9%).

Safety considerations

SSM reactions are highly exothermic (and potentially explosive) reactions that, according to theoretical calculations, can release >300 kJ mol^{-1} energy into the surrounding environment, achieving reaction temperatures of over 1000 °C in a matter of seconds. Before and during any SSM reaction, the following precautions should be taken: understand its reaction exothermicity and adiabatic (maximum) temperature, use a protective shield (outer closed container) around the reaction vessel, and

run new reactions on a small scale (<1 gram of reactants) until the energetic hazards are better understood.

Rapid SSM synthesis of CoB, FeB, and $Co_{1-x}Fe_xB$ solid solutions

CoB and FeB were synthesized using three-component displacement and redox reactions between $CoCl_2$ or $FeCl_2$ with Mg/B mixtures as we previously reported.[62] The total mass of the reactants used was approximately one gram. Typical reactant amounts used for CoB and FeB formation were 6 mmol MCl_2 ($CoCl_2$ or $FeCl_2$) with 6 mmol Mg and 12 mmol B. In the case of $Co_{1-x}Fe_xB$ solid solution synthesis, four-component displacement and redox reactions between $CoCl_2/FeCl_2$ and Mg/B mixtures were performed. The reaction stoichiometries were chosen to produce a 1:1:1 molar ratio of $Co_{1-x}Fe_xB$, B, and $MgCl_2$ salt byproduct. The typical reactant amounts used in these SSM reactions were 5 mmol MCl_2 (($1 - x)CoCl_2 + xFeCl_2$ for x = 0.2, 0.4, 0.5, 0.6, and 0.8) with 5 mmol Mg and 10 mmol B. Because rapid SSM reactions are complete in seconds and 3 or 4 reactants are involved in the reaction, an intimate mixing of reactants was performed to promote complete and homogeneous reactions. In an argon-filled glove box, $CoCl_2$, $FeCl_2$, Mg, and B powders were added sequentially to an agate mortar and ground together for 30–40 seconds after each reactant addition to obtain a homogeneous powder mixture. The reactant mixture was transferred to a cone-shaped quartz crucible (top OD = 3.6 cm, bottom OD = 1.3 cm, height = 4.9 cm), which was placed in a cylindrical stainless-steel reactor (ID = 3.8 cm, OD = 5.0 cm, height = 6.2 cm) with a loose screwcap lid.[62] A coiled nichrome wire with five loops was connected to two electrical feedthroughs on the lid to increase contact with the reactant powder mixture. The closed reactor was moved from the glove box to a fume hood. A Variac transformer set to 15.5 V was connected to the nichrome filament and turned on for about 6–8 seconds to resistively heat the filament. Within ~3 s, resistive heating raises the temperature of the nichrome wire to 750–800 °C. Wisps of white "smoke" emerging from the reactor lid indicated reaction initiation/propagation. After the SSM reactions were cooled to near room temperature, the reactor was opened and its contents, a dark product and white salt byproduct, were ground to a fine powder. Unreacted starting materials and byproduct $MgCl_2$ were removed by washing with 50 mL of stirred 0.1 M HCl for 30 min, followed by washing with 100 mL distilled water for 30 min. After each washing step, the product powders were isolated by centrifugation. The products were oven-dried for 20 minutes in air at 130 °C and mass yields were calculated using the recovered product mass and theoretical masses of metal boride products.

Sample characterization

Powder X-ray diffraction (XRD) was performed to characterize the structure and crystallinity of mixed metal boride products using a Bruker D8 DaVinci diffractometer with nickel-filtered Cu Kα X-ray irradiation (40 kV, 40 mA) from 5–80 degrees 2θ (0.05° step size). Ground metal boride powders were placed on a vacuum greased glass slide. Reference XRD patterns and crystal structure representations were generated using Crystal-Maker software (https://www.crystalmaker.com/index.html) and literature data for orthorhombic FeB, CoB, and $Co_{0.5}Fe_{0.5}B$.[68–70] CrystalDiffract software was used to match experimental data to simulated ternary $Co_{1-x}Fe_xB$ diffraction patterns based on a $Co_{0.5}Fe_{0.5}B$ crystal reference pattern (PDF 01-079-2846) (https://www.crystaldiffract.com/index.html). The morphologies and particle sizes of the products were identified using a Hitachi S-4800 field emission scanning electron microscopy (SEM) at 2–3 kV and Hitachi S-7800 transmission electron microscopy (TEM) with an accelerating voltage of 80 kV. Ground samples were affixed to carbon tape on aluminum stubs for SEM analysis or sonicated in methanol and drop cast on carbon coated Ni mesh grids for TEM analysis. Energy dispersive spectroscopy (EDS) with SEM was used to perform semiquantitative analysis of Co/Fe ratios and qualitative element specific mapping on bulk powders by metal borides affixed to carbon wax electrode tips. X-ray fluorescence spectroscopy (XRF) was used to further evaluate the quantitative elemental analysis of mixed metal borides (Rigaku ZSX Primus IV dispersive X-ray fluorescence spectrometer). Metal boride powders are compressed to 10 000 psi in a hydraulic press to form compact pellets for XRF analysis. A Quantachrome Nova 1200 nitrogen surface area analyzer was used to quantify surface areas for vacuum dried samples (120 °C for more than 3 hours). Inductively coupled plasma-optical emission spectroscopy (ICP-OES) measurements for bulk elemental analysis were performed using PerkinElmer Optima 7000 DV ICP-OES spectrometer. The metal boride samples were dissolved in heated 5 mL concentrated HNO_3 and diluted to 100 mL with 18 MΩ ultrapure water. Linear elemental calibration curves were produced from commercial ICP standards (Fe, Co, B, and Mg) diluted in 5% (v/v) HNO_3.

Working electrode preparation

Working carbon wax (C_{wax}) electrodes for electrocatalytic measurements were prepared using a graphite/paraffin wax mixture (50% graphite: 50% wax) inside PTFE tubes as previously reported by our group.[3,62,71] These C_{wax} electrodes allow direct electrocatalyst–electrolyte contact without the need for binders or conducting coatings. Working electrode tips were 1.4 cm long with a 3.2 mm ID, and 6.4 mm OD, and a 0.080 cm^2 geometrical surface area. A brass current collector rod was embedded into the blank C_{wax} electrode tip and submerged in a pre-heated water bath (55 °C) for 20 minutes prior to catalyst loading. Brief sonication of ~10 mg of the catalyst powder with 100 μL of methanol was used to make a homogeneous catalyst suspension, and ~20–30 μL aliquots were placed in an aluminum weigh boat to air dry. The air-dried catalyst-containing aluminum weigh boat was tared in a microbalance before being placed in a preheated hot plate (55 °C). The softened C_{wax} blank electrode tips were gently pressed onto the catalyst, and excess catalyst powder on the PTFE tip was carefully removed and returned to the aluminum weigh boat. The electrode tip was pressed several times in a clear space in the weigh boat to ensure that the sample powders were firmly embedded on the wax. Following catalyst loading, the aluminum weigh boat was weighed on the previously tared

microbalance, and the mass of the loaded catalyst was recorded. Sample mass loadings on the electrode typically ranged from $\sim$0.5–2.0 mg. The open end of the brass connecting rod was connected to the potentiostat (Fig. S1, ESI†).

Electrochemical measurements

Electrochemical measurements were performed in a 1.0 M KOH electrolyte solution using a three-electrode cell with a C_{wax} working electrode, Hg/HgO reference electrode (20% KOH), and a graphite rod counter electrode (Alfa Aesar, 6.2 mm diam., SPK grade, 99.9995%). The Hg/HgO electrode potential values were converted to standard hydrogen electrode potentials using the $E_{RHE} = E_{Hg/HgO} + 0.059pH + E_{0\,Hg/HgO}$, with pH = 14 and $E_{0\,Hg/HgO} = 0.098$ V. 1.0 M KOH electrolyte pH values were measured with a pH meter. All potentials are referenced to RHE values unless indicated. Reported current densities are scaled relative to the geometric area of the C_{wax} electrode (0.080 cm^2). The electrodes were attached to a PINE WaveDriver 200 bi-potentiostat and placed in a single compartment cell, which consists of a Pyrex beaker and a PTFE lid similar to our prior work.[3,62] A magnetic stir bar was placed $\sim$6 mm away from the working electrode and spun at $\sim$500 rpm throughout the electrochemical tests to remove gas bubbles (H$_2$ or O$_2$) that formed on the electrode surface. The electrolyte solutions were purged with O$_2$ or H$_2$ gases that were pre-humidified by passing them through a water bubbler. The gas purging started 30 minutes before the electrochemical measurements and lasted the duration of the experiment. The activity and stability of metal boride HER and OER were assessed using 50 linear sweep voltammograms (LSVs) in H$_2$ (ultra-high purity 99.999%, Praxair) purged electrolyte for HER or O$_2$ (99.5% purity, Praxair) purged electrolyte for OER. The LSV data were collected without iR compensation and later manually corrected for 85% iR compensation. The measured cell resistances for catalysts on C_{wax} electrodes in 1.0 M KOH were $\sim$15–30 Ω. Data for standard 10% Pt/C HER and RuO$_2$ OER catalysts on C_{wax} electrodes were obtained for comparison.

The long-term activity of the metal borides as HER and OER catalysts was investigated using 24 hour time base chrono-amperometry studies (CA) at constant potentials in 1.0 M KOH with selected applied potentials targeting a current density of $\sim$10 mA cm^{-2}. The electrochemical surface areas (ECSA) of each metal boride were determined by measuring the double-layer capacitance (C_{dl}) in the non-faradaic region (-100 to 300 mV $vs.$ RHE) with H$_2$ gas purging before HER CA measurements. ECSA analysis was performed using cyclic voltammetry (CV) data at scan rates of 10, 25, 50, 75, and 100 mV s^{-1}. Calculated capacitance values were converted to approximate areas using a 35 μF cm^{-2} relationship.[72]

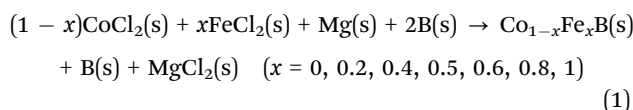### Post-electrochemistry analysis of metal boride catalyst particles on C_{wax} electrodes

The crystallinity of CoB, FeB, and Co$_{1-x}$Fe$_x$B catalysts on C_{wax} electrode tips after 24 h CA experiments was examined using powder XRD (27–60° 2θ, 0.02° step size). XRD samples were prepared from post-electrochemical electrodes by cutting

$\sim$1 mm slices from the end of the C_{wax} electrode with a thin surface coating of embedded metal boride powders and placing them in the well of an XRD sample holder for XRD analysis. SEM imaging and EDS mapping were also obtained for the catalysts embedded on C_{wax} after CA experiments. XRD and EDS mapping for metal boride powders embedded on C_{wax} electrode tips prior to electrochemical use were also collected for comparison.

Results and discussion

Solid-solution Co$_{1-x}$Fe$_x$B metal boride synthesis via SSM reactions

Previous studies have shown that solvent-free rapid ignition SSM reactions are effective for the synthesis of several binary transition-metal borides (Table S1, ESI†). The formation of a highly stable ($\Delta H_f = -644$ kJ mol^{-1}) MgCl$_2$ salt in addition to the metal boride product drives these SSM reactions. Most reported SSM reactions for MB$_x$ synthesis use an MgB$_2$ reactant and furnace heating to overcome reaction activation energies and promote atom diffusion and boride crystallization. Some challenges with rapid ignition SSM reactions are the potential for heterogeneous mixing in the rapidly cooled product and non-propagation for stable reactants with high activation energies or for low exothermicity reactions. In select cases, local ignition heating can lead to successful self-propagating SSM metal boride reactions, such as in our prior work with MCl$_2$ reacting with either MgB$_2$ or Mg/2B mixtures to form FeB, NiB, and CoB.[62] The Mg/2B reactions are more exothermic than corresponding MgB$_2$ reactions and result in high yields of crystalline metal borides. In this study, we demonstrate the successful use of exothermic ignition SSM reactions between well-mixed MCl$_2$/Mg/B reactants for the rapid formation of crystalline Co$_{1-x}$Fe$_x$B solid solution borides. The SSM reactions targeting CoB, FeB, and Co$_{1-x}$Fe$_x$B solid solutions are salt-balanced to form MgCl$_2$ (eqn (1)).

$$(1-x)CoCl_2(s) + xFeCl_2(s) + Mg(s) + 2B(s) \rightarrow Co_{1-x}Fe_xB(s)$$
$$+ B(s) + MgCl_2(s) \quad (x = 0, 0.2, 0.4, 0.5, 0.6, 0.8, 1)$$
$$(1)$$

Consistent with our prior rapid SSM metal boride work, these rapid SSM reactions were performed with excess amorphous boron reactant as it is necessary to produce single-phase CoB and FeB from rapid MCl$_2$/Mg/2B reactions and avoid metal-rich phases ($e.g.$, Fe$_2$B).[62] Most of the excess boron in the product remains as inert amorphous boron rather than being converted to soluble forms of boron such as B$_2$O$_3$ or BCl$_3$.[62] The exothermic reactions between mixed metal reactants shown in eqn (1) should achieve a molten salt intermediate state allowing for rapid reaction, heating, and crystallization of metal borides as shown schematically in Fig. 1. A range of elemental or ionic intermediates may be present in the hot wavefront.

The wide compositional range of SSM reactions described by eqn (1) all rapidly initiate and enter a self-propagating state, yielding a dark product and a white MgCl$_2$ transport (Fig. 2A and B).
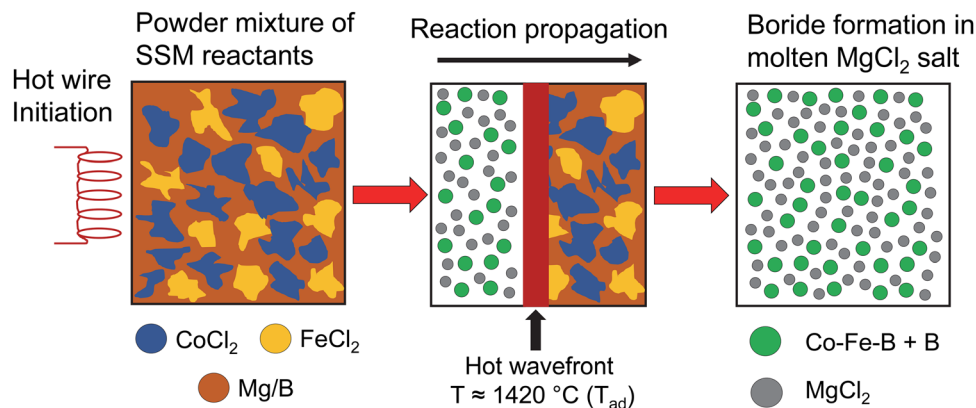
Fig. 1 Illustration of hot wire initiation of mixtures of cobalt and iron dichlorides with magnesium reductant and amorphous boron in a rapidly self-propagating and exothermic SSM reaction.

A series of black to brown products were isolated after 0.1 M HCl and DI water washing (Fig. 2C). A wide range of crystalline $Co_{1−x}Fe_xB$ materials (x = 0.2, 0.4, 0.5, 0.6, 0.8) were rapidly synthesized in high yields (>80%) using varying ratios of $CoCl_2$ and $FeCl_2$ with Mg/2B balanced SSM reactions according to eqn (1).

The single metal (x = 0 or 1) Mg/2B reactions produce CoB (PDF 04-003-2122) and FeB (PDF 04-013-1637), which both crystallize in similar orthorhombic structures but with different space groups (CoB-*Pbnm*, FeB-*Pnma*, Table S2, ESI†), leading to different lattice orientations and (*hkl*) designations for some peaks (Fig. 3). One useful feature of the CoB and FeB powder X-ray diffraction (XRD) patterns that can help identify the transition of CoB to FeB to solid-solution metal borides is that overlapped (111) and (120) XRD peaks at 41.3° in CoB systematically separate into two (111) and (201) peaks with the incorporation of iron into the $Co_{1−x}Fe_xB$ structure.
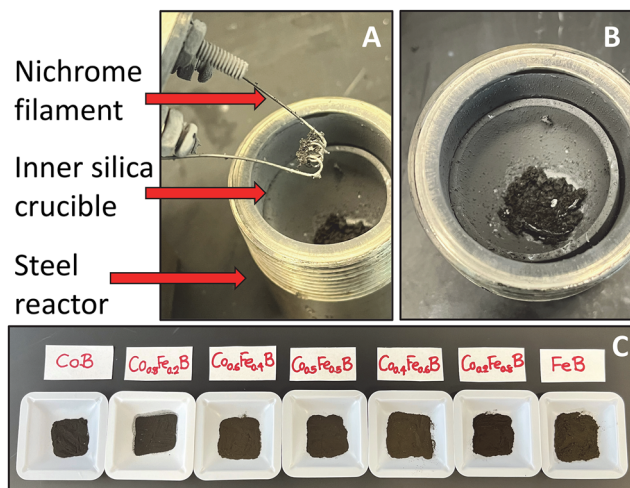

Fig. 2 (A) After SSM reaction completion, some metal boride product particles are fused to the nichrome ignition wire. (B) Black metal boride particles are at the bottom of the reaction vessel with white $MgCl_2$ deposits. (C) Images of black to brown $Co_{1−x}Fe_xB$ products ranging from CoB (far left) to FeB (far right) with solid solutions in between these end members.
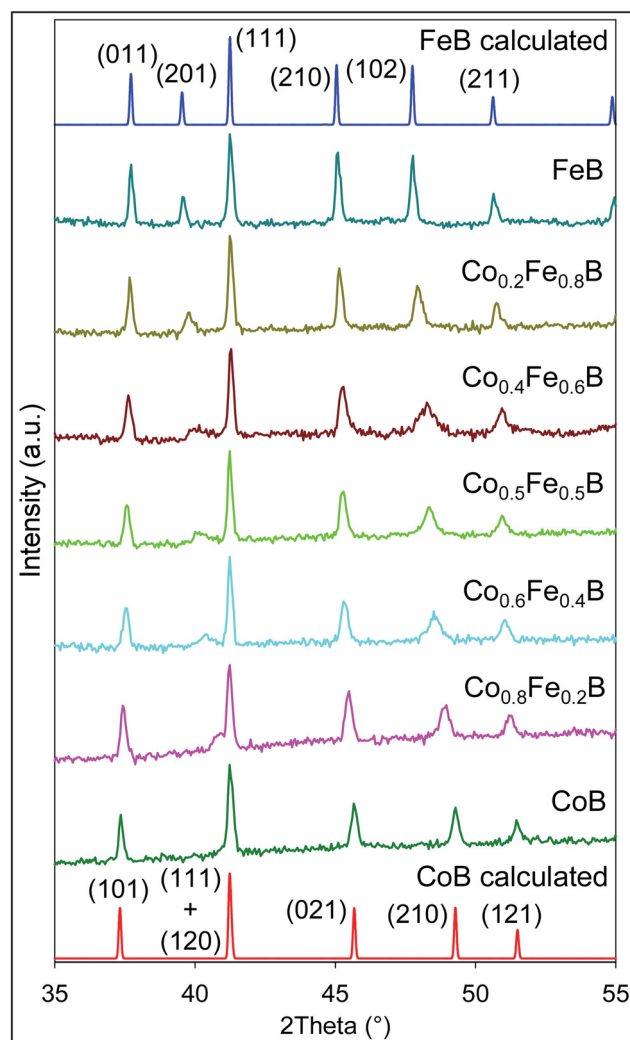

Fig. 3 Powder XRD stack plot of orthorhombic CoB, FeB, and $Co_{1−x}Fe_xB$ solid solutions. Miller indices (*hkl*) are listed for FeB and CoB end members.

Powder XRD shows the $Co_{1−x}Fe_xB$ products each appear as single-phase structures with expected peak shifts for solid-

solution mixing (Fig. 3). XRD peak positions of synthesized $Co_{1-x}Fe_xB$ solid solution products shift from CoB and FeB peak positions with increasing iron in the reactant mixture, but overall XRD patterns are comparable to CoB and FeB end members. A literature reference pattern for $Co_{0.5}Fe_{0.5}B$ (PDF 01-079-2846) is a very good match to SSM synthesized $Co_{0.5}Fe_{0.5}B$ (Table S2 and Fig. S2, ESI†) and this structure was used as the basis for determining the lattice parameters from XRD peak positions of the other $Co_{1-x}Fe_xB$ products (Tables S2 and S3, ESI†). The systematic shifting of XRD peak positions and lattice parameters with changes in ideal x value in $Co_{1-x}Fe_xB$ is shown graphically in Fig. 4, where two lattice parameters decrease and one increases with increases in cobalt content, leading to a net decrease in unit cell volume (and as expected from atomic radii Fe > Co). A plot of unit cell parameters *versus* ideal Co content shows a linear correlation (Fig. 4) and a Vegard's law like composition/lattice parameter dependence that supports the successful formation of a full range of $Co_{1-x}Fe_xB$ solid solutions from these rapid SSM reactions. To our knowledge, this is the first study that demonstrates crystalline solid-solution metal boride formation from rapid ignition SSM reactions.

A summary of SSM reactant molar ratios, isolated yields, surface areas, crystallite sizes, and bulk $Co_{1-x}Fe_xB$ chemical composition by ICP-OES analysis is shown in Table 1. Bulk elemental analysis shows that total metal (Co + Fe) *versus* B atomic ratios are close to expected ratios based on SSM production formation (MB + B or M : B = 33 : 67). There is lower

than ideal excess boron in some cases, perhaps due to loss during the wash process if MgB_x side products were formed. The Co/Fe ratios of different $Co_{1-x}Fe_xB$ products closely agree with the SSM reactant Co/Fe ratios. XRF and EDS composition metals analysis of Co and Fe similarly show product metal ratios are close to the SSM reactant ratios (Table S4, ESI†). Plots of ICP and EDS compositions *versus* unit cell volume resulted in similar linear correlations to those shown above for the ideal solid-solution concentrations (Fig. S3, ESI†).

The distribution of Co, Fe, and B was examined using SEM-EDS elemental mapping and confirmed that a relatively uniform distribution of metals and boron exists in these $Co_{1-x}Fe_xB$ products (Fig. 5). These EDS elemental maps qualitatively show a decrease in Co with increasing Fe as x increases in $Co_{1-x}Fe_xB$ products. There are regions where boron is abundant and the metal content is low, which could be excess amorphous boron present in these washed products.

SEM imaging was used to investigate the morphology and particle size distribution of the different metal borides from these rapid SSM reactions that theoretically reach temperatures near 1400 °C and grow from molten $MgCl_2$. As shown in Fig. 6 and Fig. S4, S5 (ESI†), FeB and iron-rich borides are primarily composed of round and relatively smooth particles with some that have well-defined-edges, and these particles form large 5–50 μm aggregates. The CoB and cobalt-rich solid-solution products show large (∼25–50 μm) monolithic blocky aggregates with some smaller (∼3–5 μm) particles forming sheet-like aggregates (Fig. 6 and Fig. S4, S5, ESI†). While moving from Fe-rich to Co-rich appears to alter the larger particle morphologies from round particles to faceted blocks, all products have small particle sheet-like aggregates (Fig. S4, ESI†). These sheets often have holes in them that may be a consequence of metal boride growth in molten $MgCl_2$, and holes represent areas where $MgCl_2$ was removed during washing.

The bulk gas adsorption BET surface areas for these SSM synthesized $Co_{1-x}Fe_xB$ are all relatively low (<20 m² g⁻¹) and consistent with the aggregated SEM images (Table 1). There appears to be a slight increase in surface area for the middle of the solid-solution series, with iron-rich samples showing relatively higher BET values. Since the amount of amorphous boron (BET SA = 12 m² g⁻¹) is similar in these different products, it is likely that the observed differences are related to the aggregation of the boride particles.

As shown in Table 1 (and Table S5, ESI†), the metal boride XRD average crystallite sizes are in the range of ∼50 to 70 nm, which is much smaller than the particulate sizes observed by SEM. TEM images from alcohol suspensions of smaller particles in several products show that FeB particles are nearly spherical with ∼100 to 200 nm diameters, while CoB and other solid-solution particles are irregular agglomerated nanoparticles in the 100 nm range (Fig. S6 and S7, ESI†). There is a wide range of aggregated particle sizes (∼50–400 nm), as well as semi-transparent and irregular wrinkled layer-like regions that are similar to amorphous boron (Fig. S7, ESI†). Excess boron in metal boride products is likely physically distributed throughout the sample.
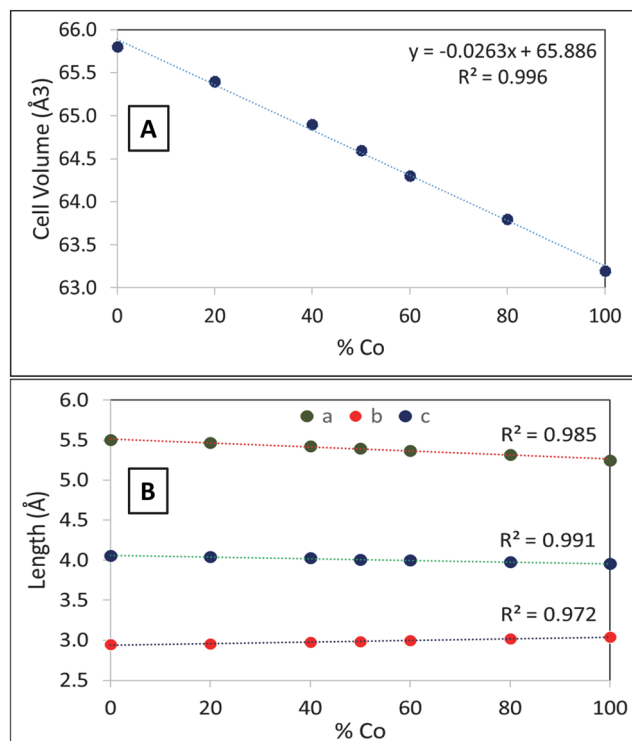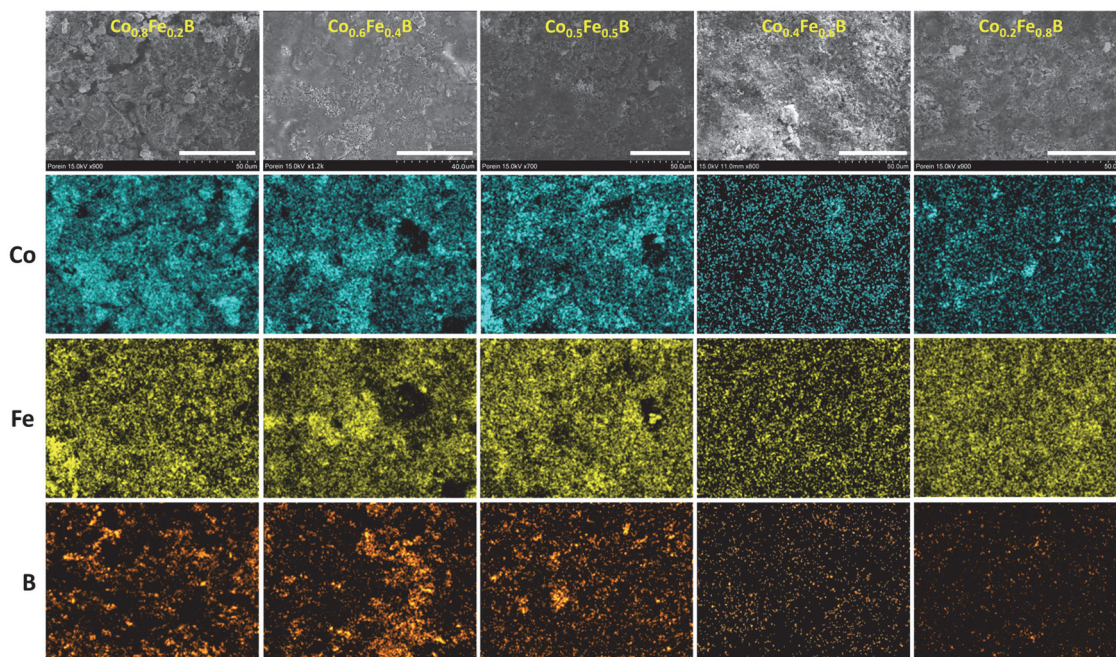

Fig. 4 Ideal percent Co in $Co_{1-x}Fe_xB$ *versus* (A) unit cell volume, (B) unit cell parameters (*a*, *b*, *c*). Linear regression lines for each data set are shown as dashed lines.

Table 1 Characterization results for $Co_{1-x}Fe_xB$ formed from $CoCl_2/FeCl_2/Mg/B$ SSM reactions

SSM reaction molar ratios	Ideal product (% yield)	ICP (at%) Co/Fe/B/Mg $Co_{1-x}Fe_xB + B^a$	BET ($m^2\ g^{-1}$)	Crystallite size (nm)
$CoCl_2/Mg/2B$	CoB + B (85)	35/0/64/1 CoB + 0.83B	2	48
$0.8CoCl_2/0.2FeCl_2/Mg/2B$	$Co_{0.8}Fe_{0.2}B$ + B (81)	34/8/56/2 $Co_{0.81}Fe_{0.19}B$ + 0.33B	3	50
$0.6CoCl_2/0.4FeCl_2/Mg/2B$	$Co_{0.6}Fe_{0.4}B$ + B (81)	19/14/65/1 $Co_{0.58}Fe_{0.42}B$ + 0.91B	11	60
$0.5CoCl_2/0.5FeCl_2/Mg/2B$	$Co_{0.5}Fe_{0.5}B$ + B (80)	16/17/66/1 $Co_{0.48}Fe_{0.52}B$ + 1.0B	11	70
$0.4CoCl_2/0.6FeCl_2/Mg/2B$	$Co_{0.4}Fe_{0.6}B$ + B (83)	13/22/64/1 $Co_{0.37}Fe_{0.63}B$ + 0.83B	17	60
$0.2CoCl_2/0.8FeCl_2/Mg/2B$	$Co_{0.2}Fe_{0.8}B$ + B (86)	6/29/64/1 $Co_{0.17}Fe_{0.83}B$ + 0.83B	8	65
$FeCl_2/Mg/2B$	FeB + B (104)	0/37/63/0 FeB + 0.70B	9	65

^{a} Product formulas calculated assuming monoboride (MB) formation with excess boron.

Fig. 5 EDS elemental mapping images of $Co_{1-x}Fe_xB$ solid-solutions showing the transition from cobalt-rich to iron-rich products (left to right). The white scale bar in the SEM images is 40 μm for $Co_{0.6}Fe_{0.4}B$ and 50 μm for other solid-solutions.

Thermochemical exothermicity and temperature predictions for metal borides

Reaction thermochemistry plays a vital role in SSM reactions because the reaction enthalpy (ΔH_{rxn}) must be significantly large and negative for the reaction to efficiently self-propagate and self-heat. A thermochemical analysis of reaction intermediate steps can provide information on favored intermediates and predict an ideal maximum reaction temperature assuming adiabatic conditions (T_{ad}). The enthalpy values and predicted temperatures (ΔH_{rxn}, T_{ad}) for metal boride formation from $MCl_2/Mg/2B$ were calculated using Hess's law and product heat capacities/phase changes, assuming complete reaction and that

reaction enthalpy released is used to heat the products (MB, B, and $MgCl_2$). Thermochemical values for $Co_{1-x}Fe_xB$ solid-solutions were estimated using end member data in ratios of $(1 - x)CoB$ and $xFeB$. A sample ΔH_{rxn} graph and T_{ad} calculation are shown in Fig. S8 (ESI†) (and associated text). All $Co_{1-x}Fe_xB$ formation reactions are predicted to reach the $MgCl_2$ boiling point (1412 °C) and have sufficient additional enthalpy to evaporate much of the $MgCl_2$ salt (Table 2).[73–76]

Stable $MgCl_2$ formation (ΔH_f = −644 kJ mol^{-1}) drives highly exothermic and self-sustaining metal boride SSM reactions. The byproduct $MgCl_2$ salt (mp/bp = 707/1412 °C) undergoes two energy absorbing melting and boiling phase transitions
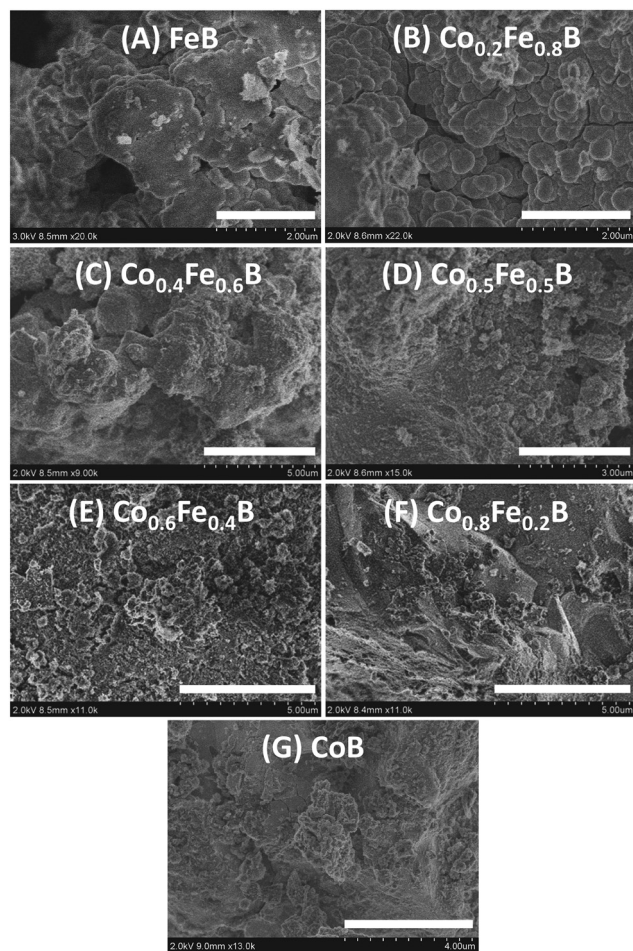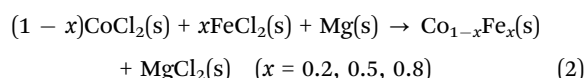
Fig. 6 Comparison of SEM particle morphologies for CoB, FeB and $Co_{1-x}Fe_xB$ solid-solutions. Scale bar lengths are: (A) 2 μm, (B) 2 μm, (C) 5 μm, (D) 3 μm, (E) 5 μm, (F) 5 μm, (G) 4 μm.

that moderate reaction temperatures. A majority of the released enthalpy is absorbed during $MgCl_2$ melting and vaporization (Fig. S8, ESI†). The molten $MgCl_2$ salt also functions as a short-lived flux that can assist in metal boride growth by providing a medium for facile diffusion of reactants to form small boride particles that can aggregate and are later encased in a solidified salt matrix.

Evaluation of metal boride SSM reaction intermediates

Previous SSM studies have proposed that SSM reactions progress through the formation of transient elemental intermediates via

ionic exchange reactions.[47,48] SSM reactions appear to progress through at least two formation energy barriers, the first being byproduct salt formation (E_{a1}), followed by product formation (E_{a2}).[48,61] The rapid self-propagation nature of SSM reactions makes a direct study of reaction mechanisms and reaction intermediates challenging.[48,52] We previously demonstrated in FeB, CoB, and NiB formation from rapid SSM reactions that the salt byproduct formation reaction ($MCl_2 + Mg \rightarrow M + MgCl_2$) is sufficient to overcome the E_{a1} activation barrier, whereas the product formation ($M + B \rightarrow MB$) requires high temperature heating to proceed.[62] In the Co–Fe–B mixed metal boride reactions, three intermediate metal salt reduction reactions were examined (eqn (2)). All these three reduction reactions are highly exothermic (>300 kJ mol^{-1}) (Table S6, ESI†).

$$(1-x)CoCl_2(s) + xFeCl_2(s) + Mg(s) \rightarrow Co_{1-x}Fe_x(s)$$
$$+ MgCl_2(s) \quad (x = 0.2, 0.5, 0.8) \quad (2)$$

Hot filament SSM reactions were successfully initiated and self-propagated to form elemental Co and Fe, though some XRD peak shifts and peak shoulders indicate that some metal mixing occurs in the products (Fig. S9, ESI†). XRD shows no Co peak in the 20% Co reaction, but EDS elemental mapping and semi-quantitative elemental analysis confirm the presence of Co near the targeted ratio (Fig. S10, ESI†). SEM analysis shows that an 80% Co sample consists of monolithic blocks (20–200 μm) and aggregates of small nanometer-sized particles, while Fe-rich particle morphologies are mainly aggregated particles (5–50 μm) (Fig. S11, ESI†). These results support the idea that exothermic metal reduction and salt formation are thermochemically favored as initial steps in these rapid SSM reactions.

Examination of electrocatalytic water splitting with Co–Fe–B mixed metal borides

Hydrogen evolution reaction (HER) electrocatalysis with metal borides

Several metal borides have been examined as HER electrocatalysts, but many prior studies use products that are nanostructured, supported, or poorly crystalline or amorphous (see Table S7 for literature summary of HER electrocatalysis using Fe/Co borides and other element crystalline borides, ESI†). Some Co–Fe–B mixed-metal boride nanoparticles show enhanced HER activity versus either CoB or FeB that are described as

Table 2 Thermochemical data on the formation of $Co_{1-x}Fe_xB$ solid solutions from $CoCl_2/FeCl_2/Mg/B$ reactions

Reaction	Targeted product	ΔH_{rxn} (kJ mol^{-1} MB)	T_{ad} (°C)	% $MgCl_2$ vaporized
$CoCl_2 + Mg + 2B$	$CoB + B + MgCl_2$	−425.8	1412	100
$0.8CoCl_2 + 0.2FeCl_2 + Mg + 2B$	$Co_{0.8}Fe_{0.2}B + B + MgCl_2$	−415.7	1412	94
$0.6CoCl_2 + 0.4FeCl_2 + Mg + 2B$	$Co_{0.6}Fe_{0.4}B + B + MgCl_2$	−405.6	1412	89
$0.5CoCl_2 + 0.5FeCl_2 + Mg + 2B$	$Co_{0.5}Fe_{0.5}B + B + MgCl_2$	−400.6	1412	86
$0.4CoCl_2 + 0.6FeCl_2 + Mg + 2B$	$Co_{0.4}Fe_{0.6}B + B + MgCl_2$	−395.6	1412	83
$0.2CoCl_2 + 0.8FeCl_2 + Mg + 2B$	$Co_{0.2}Fe_{0.8}B + B + MgCl_2$	−385.5	1412	77
$FeCl_2 + Mg + 2B$	$FeB + B + MgCl_2$	−375.4	1412	72

synergistic effects of both Co and Fe in the structure and on the surface.[11] We examined the HER activities of crystalline Co_{1-x}-Fe_xB from SSM reactions in H_2 saturated 1.0 M KOH and compared their activities to the FeB and CoB end members. Representative linear sweep voltammetry (LSV) plots show that the HER activity of SSM synthesized CoB and FeB is comparable to our previous report showing that these crystalline 3d metal borides are HER active (Fig. 7).[62] The crystalline CoB powder exhibits similar electrocatalytic activity to other reported crystalline and amorphous cobalt borides (Table S7, ESI†). There is no HER activity from amorphous boron alone, which is useful to see as each metal boride product contains ~50 mol% boron based on reaction balance and elemental analysis.

The HER activities of $Co_{1-x}Fe_xB$ materials show a systematic trend of increasing HER activity at lower applied potentials as more cobalt is substituted into FeB, with groupings of Co-rich (60–80% Co) and Co-poor samples (20–50% Co) (Fig. 7 and Fig. S12, ESI†). The crystalline $Co_{1-x}Fe_xB$ materials show comparable HER activity to previously reported crystalline or amorphous ternary metal borides containing Co and/or Fe (Table S8, ESI†). The overall HER activity to achieve 10 mA cm^{-2} (η_{10}) current density is ordered as $FeB < Co_{0.2}Fe_{0.8}B \sim Co_{0.4}Fe_{0.6}B \sim Co_{0.5}Fe_{0.5}B < Co_{0.6}Fe_{0.4}B \sim Co_{0.8}Fe_{0.2}B < CoB$ with applied potentials ranging from −223 mV to −395 mV. The average HER activities over multiple LSV scans are summarized in Table 3. At high current densities, the HER activity of the highest cobalt content $Co_{1-x}Fe_xB$ solid solutions are comparable to the benchmark 10% Pt/C. Graphical representations of applied potentials for several current densities (10, 20,

Fig. 7 Representative HER LSV results of CoB, FeB, and $Co_{1-x}Fe_xB$ solid-solutions. Plots for the C_{wax} and amorphous B are shown for comparison. Data was obtained using 1.0 M KOH in a three-electrode cell at 5 mV s^{-1} scan rate with Hg/HgO reference and graphite rod counter electrodes. Current densities are scaled using the geometric electrode area (0.08 cm^2).

50 mA cm^{-2}) as a function of run number are shown in Fig. S13 (ESI†). The LSV data shown in Fig. 7 is not *iR* compensated as this may obscure differences in catalyst activity due to surface charge transfer interactions.[77,78] LSV overlay results for 85% *iR* compensated data are shown in Fig. S14 (ESI†) and reported in Table 3, with ~10–15 mV lower applied potentials to achieve 10 mA cm^{-2} current densities *versus* uncompensated results. The electrochemical surface area (ECSA) trend for these metal borides is similar to physical BET surface areas (Table 1) with the solid solutions having higher ECSA than CoB. The geometric electrode area normalized LSV and the ECSA normalized data for $Co_{1-x}Fe_xB$ show the same trend of increasing HER activity as Fe is replaced by Co (Fig. S15, ESI†).

These HER electrocatalysis results for crystalline $Co_{1-x}Fe_xB$ solid-solutions demonstrate that Co–Fe mixing leads to a trend that more closely follows a compositional linear trend rather than a synergistic enhancement effect of both Fe and Co metals in the solid-solution boride. After normalizing for differences in surface area and resistance, our HER results in basic electrolyte indicate that the cobalt content of the $Co_{1-x}Fe_xB$ solid solution catalyst particles is the more relevant determining factor for increased HER activity at lower applied potentials. To investigate the effect of Co–Fe mixing on electrocatalytic activity, physical mixtures of CoB and FeB were made that mirror the chemical compositions of the $Co_{1-x}Fe_xB$ solid solutions. The HER electrocatalytic activities of these physically mixed $(1 − x)CoB/xFeB$ materials were between the FeB and CoB activities and they had lower ECSA values than the chemically mixed $Co_{1-x}Fe_xB$ materials (Table S9 and Fig. S16, ESI†). In the solid-solution and physical mixture experiments, CoB is more active despite its lower ECSA or surface area, suggesting that a major factor in HER activity is the cobalt content.

The initial LSV (Tafel) slopes can provide insight on the H_2 formation process that occurs on the catalyst surface. Three HER reactions at low coverage are a Volmer step – proton adsorption–reduction (120 mV dec^{-1}), a Heyrovsky step – hydride/proton interaction with reduction and H_2 desorption (40 mV dec^{-1}), and a Tafel step – hydride migration and H_2 desorption (30 mV dec^{-1}) in water and hydronium-ion reduction reactions.[79] At higher proton surface coverage, the Heyrovsky step may reach 120 mV dec^{-1}. The metal borides examined here have Tafel slopes around or above 120 mV dec^{-1} (105 to 177 mV dec^{-1}), indicating that initial proton adsorption and reduction processes on the boride surfaces may be rate limiting (Table 3 and Fig. S17, ESI†). The lowest Tafel slope is found for the most active CoB material and so initial proton adsorption to surface cobalt sites is likely a key reaction step in basic electrolyte. These solid-solution metal boride HER electrocatalysis results provide useful comparative data for theoretical studies on the energetics of surface hydrogen evolution reactions.

The extended electrocatalytic HER stability of $Co_{1-x}Fe_xB$ materials was examined in 1.0 M KOH at a constant potential to maintain ~10 mA cm^{-2} current density for a 24 hour period. These chronoamperometry (CA) studies show that the cobalt-rich $Co_{1-x}Fe_xB$ solid solutions show relatively constant activity

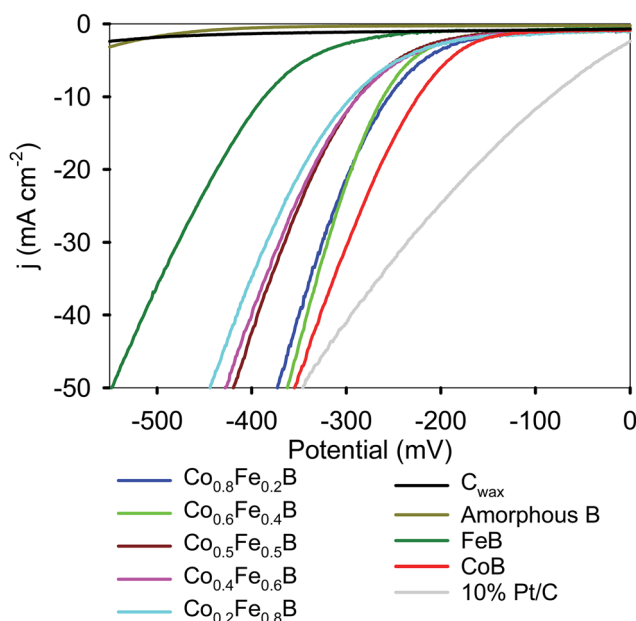**Table 3** Summary of HER electrocatalysis using SSM synthesized Co–Fe–B metal borides

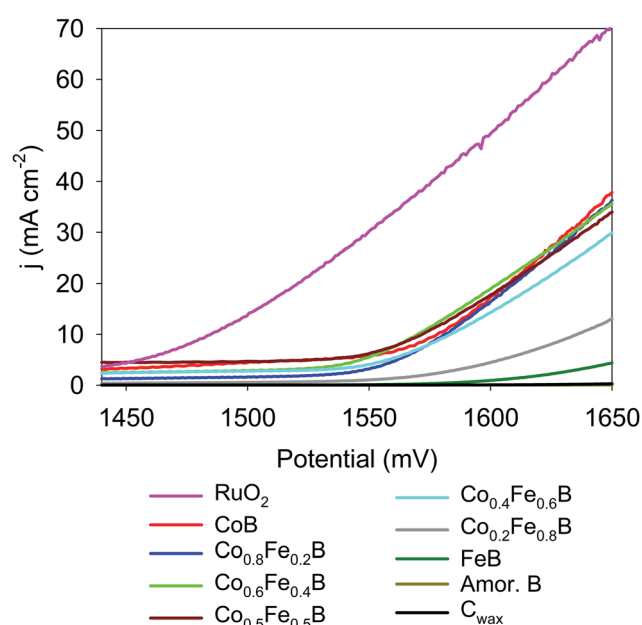| Sample	$(\eta_{10})^a$ (mV)	$(\eta_{20})^a$ (mV)	Tafel (mV dec^{-1})	ECSA (cm^2)
CoB	-223 ± 4 (-211 ± 4)	-265 ± 4 (-240 ± 4)	-105 (-90)	22
Co$_{0.8}$Fe$_{0.2}$B	-262 ± 10 (-249 ± 10)	-304 ± 11 (-278 ± 10)	-136 (-103)	31
Co$_{0.6}$Fe$_{0.4}$B	-260 ± 6 (-250 ± 7)	-294 ± 6 (-274 ± 6)	-103 (-82)	52
Co$_{0.5}$Fe$_{0.5}$B	-289 ± 10 (-274 ± 10)	-333 ± 11 (-303 ± 11)	-150 (-117)	49
Co$_{0.4}$Fe$_{0.6}$B	-289 ± 11 (-275 ± 11)	-338 ± 11 (-310 ± 11)	-160 (-131)	56
Co$_{0.2}$Fe$_{0.8}$B	-297 ± 4 (-286 ± 4)	-350 ± 3 (-327 ± 3)	-177 (-150)	52
FeB	-395 ± 3 (-382 ± 3)	-444 ± 3 (-418 ± 3)	-136 (-120)	43
B	n/a	n/a	—	3
10% Pt/C	$-83 \pm$ sss24 (-62 ± 24)	-163 ± 34 (-120 ± 34)	-89 (-83)	34

^{a} Applied potentials reported *versus* RHE in 1.0 M KOH and current densities normalized to geometric electrode area of 0.08 cm^2 (85% manual *iR* compensation results in parentheses). Deviations are for 50 LSV runs with no iR compensation and with 85% manual *iR* compensation. n/a means not achieved.

similar to CoB (Fig. S18, ESI†). The iron-rich Co$_{1-x}$Fe$_x$B and FeB show a small increase in activity over the 24 hour period that is also evident in LSVs taken after the CA experiments (Table S10, ESI†). SEM particle morphologies of FeB after CA experiments show smoother particles with fewer edges than prior to electrochemistry (Fig. S19, ESI†), indicating that some surface chemical and physical changes occur on iron-rich boride surfaces. The bulk crystallinity of the post-CA samples on electrode tips was examined by XRD and all Co$_{1-x}$Fe$_x$B samples showed key XRD peaks for their original metal boride structures, indicating the bulk structure survives extended HER reactions in 1 M KOH (Fig. S20, ESI†). EDS elemental maps of metal borides on C$_{wax}$ electrodes after extended HER electrochemistry experiments show that metal and boron are still present and distributed uniformly on the electrode surface (Fig. S21 and S22, ESI†). While it is difficult to get quantitative compositional data from the small amount of metal boride on these electrode tip samples, EDS analysis suggests that some samples may lose cobalt relative to iron after extended 24 hour cycling (Table S11, ESI†), even when bulk XRD structures remain intact.

OER electrocatalysis using metal borides

The literature evidence suggests that Fe is important in Co–Fe-solid solution OER electrocatalysts, but the precise function of Fe is not well understood. Post-electrochemistry XPS results confirm that Fe compounds readily form OOH-like species that may increase the catalytic activity of Co$_x$–Fe–B.[65] Active surface oxygen species thought to play an important role in OER catalysis include Co(O)OH, Fe(O)OH, and FeCo(O)OH.[11,65,66] The OER activities of crystalline Co$_{1-x}$Fe$_x$B solid-solutions were examined in this study to investigate the influence of Fe mixing with Co in borides on OER electrocatalytic activity as compared to activities of the CoB and FeB end members. Representative metal boride LSVs are shown in Fig. 8 and illustrate CoB and Co-rich Co$_{1-x}$Fe$_x$B solid-solutions possess higher OER activity as compared to FeB and Fe-rich Co$_{0.2}$Fe$_{0.8}$B samples (Fig. S23, ESI†). Very similar OER activity is seen for CoB and Co$_{1-x}$Fe$_x$B solid-solutions up to ~40 at% Co with only a ~14 mV potential difference at 10 mA cm^{-2} current density.

Initial LSV scans for several samples show Co^{2+} to Co^{3+} oxidation peaks, likely creating CoOOH surface species.[80]

Fig. 8 Representative OER LSV results of CoB, FeB, and Co$_{1-x}$Fe$_x$B solid-solutions. Plots for the C$_{wax}$ and boron are shown for comparison. Data was obtained in O$_2$ purged 1.0 M KOH in a three-electrode cell at 5 mV s^{-1} scan rate with Hg/HgO reference and graphite rod counter electrodes. Current densities are scaled using the geometric electrode area (0.08 cm^2). Amorphous boron and C$_{wax}$ data are at baseline levels.

Six LSVs were performed as conditioning runs to achieve reproducible, overlapping LSVs (Fig. S24, ESI†). This Co^{2+} oxidation peak shifts to higher potentials with Fe incorporation and decreases in magnitude (Fig. S25, ESI†), which could indicate some redox interactions between Co and Fe in Co$_{1-x}$Fe$_x$B.[65] The average applied potentials to achieve 10 and 20 mA cm^{-2} current densities are reported in Table 4 and show similar OER activities for CoB and the Co$_{1-x}$Fe$_x$B solid solutions with $x \geq 0.4$ with relatively stable OER over multiple LSV runs with and without *iR* compensation (Fig. S26 and S27, ESI†). Based on the LSVs results, there is no evidence for a synergistic Fe–Co enhancement of OER activity with these crystalline solid solutions *versus* a more systematic trend of higher Co content leading to higher OER activity. As shown in Fig. 8, once the solid-solution material reaches ~50 mol%

Table 4 Summary of OER electrocatalysis of SSM synthesized metal borides

Sample	Applied potential@ 10 mA cm^{-2} (mV)^a	Applied potential@ 20 mA cm^{-2} (mV)^a	Tafel (mV dec^{-1})
CoB	1575 ± 12 (1562 ± 12)	1608 ± 1 (1581 ± 1)	95 (55)
Co$_{0.8}$Fe$_{0.2}$B	1581 ± 5 (1568 ± 5)	1609 ± 6 (1583 ± 6)	66 (44)
Co$_{0.6}$Fe$_{0.4}$B	1570 ± 2 (1553 ± 2)	1603 ± 3 (1569 ± 3)	79 (49)
Co$_{0.5}$Fe$_{0.5}$B	1568 ± 17 (1553 ± 17)	1607 ± 6 (1578 ± 6)	103 (68)
Co$_{0.4}$Fe$_{0.6}$B	1583 ± 7 (1568 ± 7)	1618 ± 9 (1590 ± 9)	87 (63)
Co$_{0.2}$Fe$_{0.8}$B	1633 ± 10 (1616 ± 10)	1675 ± 13 (1640 ± 13)	78 (67)
FeB	1686 ± 4 (1673 ± 4)	1735 ± 6 (1707 ± 6)	52 (51)
RuO$_2$	1484 ± 3 (1469 ± 3)	1520 ± 3 (1489 ± 3)	99 (68)
B	n/a	n/a	3

^{a} Applied potentials reported *versus* RHE in 1.0 M KOH and current densities normalized to geometric electrode area of 0.08 cm^2 (85% manually calculated *iR* compensation results in parentheses). Deviations are for 50 LSV runs with and without *iR* compensation, after 6 conditioning runs. n/a means current density not achieved.

Co content, the OER activity is similar to the activity of the CoB end member.

The extended 24 hour OER activities of CoB, FeB, and Co$_{1-x}$Fe$_x$B solid-solutions were examined in 1.0 M KOH using CA experiments with a set potential to maintain ∼10 mA cm^{-2} current density. While the cobalt-containing metal borides display very good overall extended OER stability, the less active FeB exhibits some improved OER electrocatalytic activity over time (Fig. S28 and Table S12, ESI†). The post-CA analysis of catalyst particles on electrode tips shows that the bulk crystallinity of the metal borides is retained after extended oxidizing electrocatalysis (Fig. S20, ESI†). EDS elemental maps show that a relatively uniform distribution of metal and B on the catalyst surface remains after extended CA experiments, with higher surface oxygen as expected (Fig. S29, ESI†). The Co/Fe metal ratio of Co$_{1-x}$Fe$_x$B solid-solutions is similar to those of the starting boride catalyst, indicating these boride solid solution materials are fairly robust even if some surface oxyhydroxide formation occurs (Table S11, ESI†).

Conclusions

In this study, we demonstrated that the solvent-free, rapid and exothermic SSM reactions produce crystalline Co$_{1-x}$Fe$_x$B solid-solution metal borides with compositions that reflect the stoichiometric ratios of CoCl$_2$, FeCl$_2$, Mg, and B reactants. This work highlights the successful atomic level mixing and reaction of four reactants in a hot filament initiated rapid (few seconds) SSM reactions leading to metal boride crystal growth in molten MgCl$_2$ where reaction temperatures may transiently reach ∼1400 °C. This four-component SSM reaction successfully produced crystalline Co$_{1-x}$Fe$_x$B compositions with a wide range of x values (x = 0, 0.2, 0.4, 0.5, 0.6, 0.8, 1). The changes in unit cell parameters follow a nearly linear relationship with compositional changes in Co$_{1-x}$Fe$_x$B. An examination of reaction intermediates indicates that exothermic MCl$_2$/Mg reduction reactions form metal alloys that can react with amorphous boron in the molten salt. The HER and OER activities of this series of mixed metal borides were examined in 1.0 M KOH and both show higher activity for the more cobalt-rich phases. The cobalt containing borides showed very good extended electrocatalytic stability and bulk crystallinity of Co$_{1-x}$Fe$_x$B on carbon wax electrodes is retained after electrocatalysis. The observed HER activity trend correlates well with cobalt composition, indicating that these crystalline microparticulate metal boride catalysts show a systematic rather than synergistic impact of iron additions to CoB. This work also provides new support for the utility of a magnesium reduction strategy for rapid SSM reactions that allows facile tuning of reaction products and mixed metal boride structures.

Author contributions

JA performed all metal boride SSM experiments, conducted all product analyses, and ran all the electrochemical experiments. JA and EG both contributed to experimental designs, manuscript preparation, and the creation of graphical and tabular content.

Conflicts of interest

There are no conflicts to declare.

Acknowledgements

References

1 S. Sharma and S. K. Ghoshal, Hydrogen the future transportation fuel: From production to applications, *Renewable Sustainable Energy Rev.*, 2015, **43**, 1151–1158, DOI: **10.1016/j.rser.2014.11.093**.

2 A. W. C. van den Berg and C. O. Arean, Materials for hydrogen storage: current research trends and perspectives, *Chem. Commun.*, 2008, 668–681, DOI: **10.1039/b712576n**.

3 N. Coleman, M. D. Lovander, J. Leddy and E. G. Gillan, Phosphorus-Rich Metal Phosphides: Direct and Tin Flux-Assisted Synthesis and Evaluation as Hydrogen Evolution Electrocatalysts, *Inorg. Chem.*, 2019, **58**(8), 5013–5024, DOI: **10.1021/acs.inorgchem.9b00032**.

4 J. Xu, J. Li, D. Xiong, B. Zhang, Y. Liu, K.-H. Wu, I. Amorim, W. Li and L. Liu, Trends in activity for the oxygen evolution reaction on transition metal (M = Fe, Co, Ni) phosphide precatalysts, *Chem. Sci.*, 2018, **9**(14), 3470–3476, DOI: **10.1039/c7sc05033j**.

5 M. S. Burke, M. G. Kast, L. Trotochaud, A. M. Smith and S. W. Boettcher, Cobalt–Iron (Oxy)hydroxide Oxygen Evolution Electrocatalysts: The Role of Structure and Composition on Activity, Stability, and Mechanism, *J. Am. Chem.*

Soc., 2015, **137**(10), 3638–3648, DOI: **10.1021/jacs. 5b00281**.

6 D. Guo, H. Kang, P. Wei, Y. Yang, Z. Hao, Q. Zhang and L. Liu, A high-performance bimetallic cobalt iron oxide catalyst for the oxygen evolution reaction, *CrystEngComm*, 2020, **22**(25), 4317–4323, DOI: **10.1039/d0ce00401d**.

7 S.-Y. Huang, D. Sodano, T. Leonard, S. Luiso and P. S. Fedkiw, Cobalt-Doped Iron Sulfide as an Electrocatalyst for Hydrogen Evolution, *J. Electrochem. Soc.*, 2017, **164**(4), F276–F282, DOI: **10.1149/2.0761704jes**.

8 Y. Zhou, M. Luo, Z. Zhang, W. Li, X. Shen, W. Xia, M. Zhou and X. Zeng, Iron doped cobalt sulfide derived boosted electrocatalyst for water oxidation, *Appl. Surf. Sci.*, 2018, **448**, 9–15, DOI: **10.1016/j.apsusc.2018.04.080**.

9 D. Li, Y. Xing, R. Yang, T. Wen, D. Jiang, W. Shi and S. Yuan, Holey Cobalt-Iron Nitride Nanosheet Arrays as High-Performance Bifunctional Electrocatalysts for Overall Water Splitting, *ACS Appl. Mater. Interfaces*, 2020, **12**(26), 29253–29263, DOI: **10.1021/acsami.0c05219**.

10 Y. Wang, D. Liu, Z. Liu, C. Xie, J. Huo and S. Wang, Porous cobalt-iron nitride nanowires as excellent bifunctional electrocatalysts for overall water splitting, *Chem. Commun.*, 2016, **52**(85), 12614–12617, DOI: **10.1039/c6cc06608a**.

11 C. Qiang, L. Zhang, H. He, Y. Liu, Y. Zhao, T. Sheng, S. Liu, X. Wu and Z. Fang, Efficient electrocatalytic water splitting by bimetallic cobalt iron boride nanoparticles with controlled electronic structure, *J. Colloid Interface Sci.*, 2021, **604**, 650–659, DOI: **10.1016/j.jcis.2021.07.024**.

12 Y. Li, B. Huang, Y. Sun, M. Luo, Y. Yang, Y. Qin, L. Wang, C. Li, F. Lv and W. Zhang, *et al.*, Multimetal Borides Nanochains as Efficient Electrocatalysts for Overall Water Splitting, *Small*, 2019, **15**, 1804212, DOI: **10.1002/smll.201804212**.

13 A. W. Weimer, *Carbide, Nitride and Boride Materials Synthesis and Processing*, Chapman and Hall, 1997.

14 Q. Gu, G. Krauss and W. Steurer, Transition Metal Borides: Superhard versus Ultra-incompressible, *Adv. Mater.*, 2008, **20**(19), 3620–3626, DOI: **10.1002/adma.200703025**.

15 B. P. T. Fokwa, Borides: Solid-State Chemistry, in *Encyclopedia of Inorganic and Bioinorganic Chemistry*, Wiley, 2014, pp. 1–14, DOI: **10.1002/9781119951438.eibc0022.pub2**.

16 P. Wang, R. Kumar, E. M. Sankaran, X. Qi, X. Zhang, D. Popov, A. L. Cornelius, B. Li, Y. Zhao and L. Wang, Vanadium Diboride (VB_2) Synthesized at High Pressure: Elastic, Mechanical, Electronic, and Magnetic Properties and Thermal Stability, *Inorg. Chem.*, 2018, **57**(3), 1096–1105, DOI: **10.1021/acs.inorgchem.7b02550**.

17 D. Demirskyi, I. Solodkyi, T. Nishimura, Y. Sakka and O. Vasylkiv, High-temperature strength and plastic deformation behavior of niobium diboride consolidated by spark plasma sintering, *J. Am. Ceram. Soc.*, 2017, **100**(11), 5295–5305, DOI: **10.1111/jace.15048**.

18 R. W. Cumberland, M. B. Weinberger, J. J. Gilman, S. M. Clark, S. H. Tolbert and R. B. Kaner, Osmium Diboride, an Ultra-Incompressible, Hard Material, *J. Am. Chem. Soc.*, 2005, **127**(20), 7264–7265, DOI: **10.1021/ja043806y**.

19 B. Aronsson, T. Lundström and S. Rundqvist, *Borides, Silicides and Phosphides*, John Wiley & Sons Inc, 1965.

20 H.-Y. Chung, M. B. Weinberger, J. B. Levine, A. Kavner, J.-M. Yang, S. H. Tolbert and R. B. Kaner, Synthesis of Ultra-Incompressible Superhard Rhenium Diboride at Ambient Pressure, *Science*, 2007, **316**(5823), 436–439, DOI: **10.1126/science.1139322**.

21 I. E. Campos-Silva and G. A. Rodríguez-Castro, Boriding to improve the mechanical properties and corrosion resistance of steels, in *Thermochemical Surface Engineering of Steels*, ed. E. J. Mittemeijer and M. A. J. Somers, Woodhead Publishing, 2015, pp. 651–702.

22 W. Hao, R. Wu, R. Zhang, Y. Ha, Z. Chen, L. Wang, Y. Yang, X. Ma, D. Sun and F. Fang, *et al.*, Electroless Plating of Highly Efficient Bifunctional Boride-Based Electrodes toward Practical Overall Water Splitting, *Adv. Energy Mater.*, 2018, **8**(26), 1801372, DOI: **10.1002/aenm.201801372**.

23 M. Zeng, H. Wang, C. Zhao, J. Wei, K. Qi, W. Wang and X. Bai, Nanostructured Amorphous Nickel Boride for High-Efficiency Electrocatalytic Hydrogen Evolution over a Broad pH Range, *ChemCatChem*, 2016, **8**(4), 708–712, DOI: **10.1002/cctc.201501221**.

24 P. R. Jothi, Y. Zhang, J. P. Scheifers, H. Park and B. P. T. Fokwa, Molybdenum diboride nanoparticles as a highly efficient electrocatalyst for the hydrogen evolution reaction, *Sustainable Energy Fuels*, 2017, **1**, 1928–1934, DOI: **10.1039/c7se00397h**.

25 P. R. Jothi, Y. Zhang, K. Yubuta, D. B. Culver, M. Conley and B. P. T. Fokwa, Abundant Vanadium Diboride with Graphene-like Boron layers for Hydrogen Evolution, *ACS Appl. Energy Mater.*, 2019, **2**(1), 176–181, DOI: **10.1021/acsaem.8b01615**.

26 F. Guo, Y. Wu, X. Ai, H. Chen, G.-D. Li, W. Chen and X. Zou, A class of metal diboride electrocatalysts synthesized by a molten salt-assisted reaction for the hydrogen evolution reaction, *Chem. Commun.*, 2019, **55**(59), 8627–8630, DOI: **10.1039/c9cc03638e**.

27 Y. Yao, Z. Zhang and L. Jiao, Development Strategies in Transition Metal Borides for Electrochemical Water Splitting, *Energy Environ. Mater.*, 2022, **5**(2), 470–485, DOI: **10.1002/eem2.12198**.

28 Z. Pu, T. Liu, G. Zhang, X. Liu, M. A. Gauthier, Z. Chen and S. Sun, Nanostructured Metal Borides for Energy-Related Electrocatalysis: Recent Progress, Challenges, and Perspectives, *Small Methods*, 2021, **5**(10), 2100699, DOI: **10.1002/smtd.202100699**.

29 S. Gupta, M. K. Patel, A. Miotello and N. Patel, Metal Boride-Based Catalysts for Electrochemical Water-Splitting: A Review, *Adv. Funct. Mater.*, 2020, **30**(1), 1906481, DOI: **10.1002/adfm.201906481**.

30 Y. Jiang and Y. Lu, Designing transition-metal-boride-based electrocatalysts for applications in electrochemical water splitting, *Nanoscale*, 2020, **12**(17), 9327–9351, DOI: **10.1039/d0nr01279c**.

31 Z. Chen, X. Duan, W. Wei, S. Wang, Z. Zhang and B.-J. Ni, Boride-based electrocatalysts: Emerging candidates for water splitting, *Nano Res.*, 2020, **13**(2), 293–314, DOI: **10.1007/s12274-020-2618-y**.

32 H. Chen and X. Zou, Intermetallic borides: structures, synthesis and applications in electrocatalysis, *Inorg. Chem. Front.*, 2020, **7**(11), 2248–2264, DOI: **10.1039/d0qi00146e**.

33 H. Park, Y. Zhang, E. Lee, P. Shankhari and B. P. T. Fokwa, High-Current-Density HER Electrocatalysts: Graphene-like Boron Layer and Tungsten as Key Ingredients in Metal Diborides, *ChemSusChem*, 2019, **12**(16), 3726–3731, DOI: **10.1002/cssc.201901301**.

34 D. K. Mann, J. Xu, N. E. Mordvinova, V. Yannello, Y. Ziouani, N. Gonzalez-Ballesteros, J. P. S. Sousa, O. I. Lebedev, Y. V. Kolen'ko and M. Shatruk, Electrocatalytic water oxidation over AlFe₂B₂, *Chem. Sci.*, 2019, **10**(9), 2796–2804, DOI: **10.1039/c8sc04106g**.

35 S. J. Sitler, K. S. Raja and I. Charit, Metal-Rich Transition Metal Diborides as Electrocatalysts for Hydrogen Evolution Reactions in a Wide Range of pH, *J. Electrochem. Soc.*, 2016, **163**(13), H1069–H1075, DOI: **10.1149/2.0201613jes**.

36 M. Sheng, Q. Wu, Y. Wang, F. Liao, Q. Zhou, J. Hou and W. Weng, Network-like porous Co-Ni-B grown on carbon cloth as efficient and stable catalytic electrodes for hydrogen evolution, *Electrochem. Commun.*, 2018, **93**, 104–108, DOI: **10.1016/j.elecom.2018.06.017**.

37 S. Gupta, N. Patel, R. Fernandes, R. Kadrekar, A. Dashora, A. K. Yadav, D. Bhattacharyya, S. N. Jha, A. Miotello and D. C. Kothari, Co–Ni–B nanocatalyst for efficient hydrogen evolution reaction in wide pH range, *Appl. Catal., B*, 2016, **192**, 126–133, DOI: **10.1016/j.apcatb.2016.03.032**.

38 S. Klemenz, J. Schuch, S. Hawel, A. M. Zieschang, B. Kaiser, W. Jaegermann and B. Albert, Synthesis of a Highly Efficient Oxygen-Evolution Electrocatalyst by Incorporation of Iron into Nanoscale Cobalt Borides, *ChemSusChem*, 2018, **11**(18), 3150–3156, DOI: **10.1002/cssc.201801547**.

39 X. Ma, J. Wen, S. Zhang, H. Yuan, K. Li, F. Yan, X. Zhang and Y. Chen, Crystal Co$_x$B (x = 1-3) Synthesized by a Ball-Milling Method as High-Performance Electrocatalysts for the Oxygen Evolution Reaction, *ACS Sustainable Chem. Eng.*, 2017, **5**(11), 10266–10274, DOI: **10.1021/acssuschemeng.7b02281**.

40 L. T. Alameda, C. F. Holder, J. L. Fenton and R. E. Schaak, Partial Etching of Al from MoAlB Single Crystals To Expose Catalytically Active Basal Planes for the Hydrogen Evolution Reaction, *Chem. Mater.*, 2017, **29**(21), 8953–8957, DOI: **10.1021/acs.chemmater.7b02511**.

41 P. R. Jothi, K. Yubuta and B. P. T. Fokwa, A Simple, General Synthetic Route toward Nanoscale Transition Metal Borides, *Adv. Mater.*, 2018, **30**(14), 1704181, DOI: **10.1002/adma.201704181**.

42 Z. Sun, S. Hao, X. Ji, X. Zheng, J. Xie, X. Li and B. Tang, Efficient alkaline hydrogen evolution electrocatalysis enabled by an amorphous Co-Mo-B film, *Dalton Trans.*, 2018, **47**(23), 7640–7643, DOI: **10.1039/c8dt01296b**.

43 S. Wang, P. He, Z. Xie, L. Jia, M. He, X. Zhang, F. Dong, H. Liu, Y. Zhang and C. Li, Tunable nanocotton-like amorphous ternary Ni-Co-B: A highly efficient catalyst for enhanced oxygen evolution reaction, *Electrochim. Acta*, 2019, **296**, 644–652, DOI: **10.1016/j.electacta.2018.11.099**.

44 G. Gouget, P. Beaunier, D. Portehault and C. Sanchez, New route toward nanosized crystalline metal borides with tuneable stoichiometry and variable morphologies, *Faraday Discuss.*, 2016, **191**, 511–525, DOI: **10.1039/c6fd00053c**.

45 X. Liang, R. Dong, D. Li, X. Bu, F. Li, L. Shu, R. Wei and J. C. Ho, Coupling of Nickel Boride and Ni(OH)₂ Nanosheets with Hierarchical Interconnected Conductive Porous Structure Synergizes the Oxygen Evolution Reaction, *ChemCatChem*, 2018, **10**(20), 4555–4561, DOI: **10.1002/cctc.201800993**.

46 K. E. Woo, S. Kong, W. Chen, T. H. Chang, G. Viswanathan, A. M. Díez, V. Sousa, Y. V. Kolenko, O. I. Lebedev and M. Costa Figueiredo, *et al.*, Topotactic BI3-assisted boridization: synthesis and electrocatalysis applications of transition metal borides, *J. Mater. Chem. A*, 2022, **10**(40), 21738–21749, DOI: **10.1039/d2ta04266e**.

47 E. G. Gillan and R. B. Kaner, Synthesis of Refractory Ceramics via Rapid Metathesis Reactions between Solid-State Precursors, *Chem. Mater.*, 1996, **8**, 333–343, DOI: **10.1021/cm950232a**.

48 I. P. Parkin, Solid State Metathesis Reaction For Metal Borides, Silicides, Pnictides and Chalcogenides: Ionic or Elemental Pathways, *Chem. Soc. Rev.*, 1996, **25**(3), 199–207.

49 A. Wustrow and J. R. Neilson, 5.03–Metathesis routes to materials, in *Comprehensive Inorganic Chemistry III*, ed. J. Reedijk and K. R. Poeppelmeier, Elsevier, 3rd edn, 2023, pp. 24–39.

50 J. P. Abeysinghe and E. G. Gillan, Thermochemical reaction strategies for the rapid formation of inorganic solid-state materials, in *Dynamic Processes in Solids*, ed. J. E. House, Elsevier, 1st edn, 2023, pp. 51–95.

51 R. F. Jarvis, R. M. Jacubinas and R. B. Kaner, Self-Propagating Metathesis Routes to Metastable Group 4 Phosphides, *Inorg. Chem.*, 2000, **39**(15), 3243–3246, DOI: **10.1021/ic000057m**.

52 R. E. Treece, J. A. Conklin and R. B. Kaner, Metathetical Synthesis of Binary and Ternary Antiferromagnetic Gadolinium Pnictides (P, As, and Sb, *Inorg. Chem.*, 1994, **33**(25), 5701–5707, DOI: **10.1021/ic00103a016**.

53 J. C. Fitzmaurice, A. Hector and I. P. Parkin, Rapid synthesis of TiN, HfN and ZrN from solid-state precursors, *Polyhedron*, 1993, **12**(11), 1295–1300.

54 E. G. Gillan and R. B. Kaner, Rapid Solid-State Synthesis of Refractory Nitrides, *Inorg. Chem.*, 1994, **33**(25), 5693–5700, DOI: **10.1021/ic00103a015**.

55 J. B. Wiley, E. G. Gillan and R. B. Kaner, Rapid solid state metathesis reactions for the synthesis of copper oxide and other metal oxides, *Mat. Res. Bull.*, 1993, **28**(9), 893–900, DOI: **10.1016/0025-5408(93)90035-c**.

56 E. G. Gillan and R. B. Kaner, Rapid, energetic metathesis routes to crystalline metastable phases of zirconium and hafnium dioxide, *J. Mater. Chem.*, 2001, **11**(7), 1951–1956, DOI: **10.1039/b102234m**.

57 P. R. Bonneau, R. F. Jarvis and R. B. Kaner, Solid-State Metathesis as a Quick Route to Transition-Metal Mixed Dichalcogenides, *Inorg. Chem.*, 1992, **31**(11), 2127–2132, DOI: **10.1021/ic00037a027**.

58 N. Coleman, S. Perera and E. G. Gillan, Rapid solid-state metathesis route to transition-metal doped titanias, *J. Solid*

State Chem., 2015, **232**, 241–248, DOI: **10.1016/j.jssc.2015.09.028**.

59 S. Perera, N. A. Zelenski, R. E. Pho and E. G. Gillan, Rapid and exothermic solid-state synthesis of metal oxyhalides and their solid solutions via energetic metathesis reactions, *J. Solid State Chem.*, 2007, **180**(10), 2916–2925, DOI: **10.1016/j.jssc.2007.08.005**.

60 P. R. Bonneau and R. B. Kaner, High-quality mixed-transition-metal dichalcogenides from solid-state exchange reactions, *Inorg. Chem.*, 1993, **32**(26), 6084–6087, DOI: **10.1021/ic00078a028**.

61 L. Rao, E. G. Gillan and R. B. Kaner, Rapid synthesis of transition-metal borides by solid-state metathesis, *J. Mater. Res.*, 1995, **10**(2), 353–361.

62 J. P. Abeysinghe, A. F. Kolln and E. G. Gillan, Rapid and Energetic Solid-State Metathesis Reactions for Iron, Cobalt, and Nickel Boride Formation and Their Investigation as Bifunctional Water Splitting Electrocatalysts, *ACS Mater. Au*, 2022, **2**(4), 489–504, DOI: **10.1021/acsmaterialsau.1c00079**.

63 K. Patil, P. Babar, X. Li, V. Karade, S. Kim, S. Y. Jang, P. Bhoite and J. H. Kim, Co–Fe–B Nanochain Electrocatalysts for Oxygen Evolution at High Current Density, *ACS Appl. Nano Mater.*, 2022, **5**(5), 6260–6267, DOI: **10.1021/acsanm.2c00312**.

64 X. Liu, G. He, H. Liu, Y. Zhu, J. Xiao and L. Han, Boron-doped cobalt-iron bimetal phosphides nanosheets for enhanced oxygen evolution, *J. Alloys Compd.*, 2022, **893**, DOI: **10.1016/j.jallcom.2021.162208**.

65 H. Chen, S. Ouyang, M. Zhao, Y. Li and J. Ye, Synergistic Activity of Co and Fe in Amorphous Co*x*-Fe-B Catalyst for Efficient Oxygen Evolution Reaction, *ACS Appl. Mater. Interfaces*, 2017, **9**(46), 40333–40343, DOI: **10.1021/acsami.7b13939**.

66 X. Zou, W. Zhang, X. Zhou, K. Song, X. Ge and W. Zheng, The surface of metal boride tinted by oxygen evolution reaction for enhanced water electrolysis, *J. Energy Chem.*, 2022, **72**, 509–515, DOI: **10.1016/j.jechem.2022.05.0392 095-4956**.

67 J. M. V. Nsanzimana, L. Gong, R. Dangol, V. Reddu, V. Jose, B. Y. Xia, Q. Yan, J. M. Lee and X. Wang, Tailoring of Metal Boride Morphology via Anion for Efficient Water Oxidation, *Adv. Energy Mater.*, 2019, **9**(28), 1901503, DOI: **10.1002/aenm.201901503**.

68 C. Kapfenberger, B. Albert, R. Pottgen and H. Huppertz, Structure refinements of iron borides Fe$_2$B and FeB, *Z. Kristallogr.*, 2006, **221**(5–7), 477–481, DOI: **10.1524/zkri.2006.221.5-7.477**.

69 T. Bjurstrom, Rontgenanalyse der Systeme Eisen-Bor, Kobalt-Bor und Nickel-Bor, *Ark. Kemi, Mineral. Geo.*, 1933, **11A**, 1.

70 C. Gianoglio and E. Quadrini, Sul sistema cobalto-ferro-boro, *Atti Accad. Sci. Torino, Cl. Sci. Fis., Mat. Nat.*, 1980, **114**, 125.

71 N. Coleman, I. A. Liyanage, M. D. Lovander, J. Leddy and E. G. Gillan, Facile Solvent-Free Synthesis of Metal Thiophosphates and Their Examination as Hydrogen Evolution Electrocatalysts, *Molecules*, 2022, **27**(16), 5053, DOI: **10.3390/molecules27165053**.

72 C. C. McCrory, S. Jung, J. C. Peters and T. F. Jaramillo, Benchmarking heterogeneous electrocatalysts for the oxygen evolution reaction, *J. Am. Chem. Soc.*, 2013, **135**(45), 16977–16987, DOI: **10.1021/ja407115p**.

73 M. Binnewies and E. Milke, *Thermochemical Data of Elements and Compounds*, Weinheim, 1999.

74 *CRC Handbook of Chemistry and Physics*, ed. J. R. Rumble, CRC Press/Taylor & Francis, 102nd edn, 2021.

75 O. Kubaschewski and C. B. Alcock, *Metallurgical Thermochemistry*, Pergamon Press Inc., Maxwell House, 1979.

76 NIST Chemistry Webbook, Standard Reference Database, (accessed 7/5/2021).

77 L. Yu and Z. Ren, Systematic study of the influence of iR compensation on water electrolysis, *Mater. Today Phys.*, 2020, **14**, 100253, DOI: **10.1016/j.mtphys.2020.100253**.

78 S. Anantharaj, S. R. Ede, K. Karthick, S. S. Sankar, K. Sangeetha, P. E. Karthik and S. Kundu, Precision and correctness in the evaluation of electrocatalytic water splitting: revisiting activity parameters with a critical assessment, *Energy Environ. Sci.*, 2018, **11**(4), 744–771, DOI: **10.1039/c7ee03457a**.

79 T. Shinagawa, A. T. Garcia-Esparza and K. Takanabe, Insight on Tafel slopes from a microkinetic analysis of aqueous electrocatalysis for energy conversion, *Sci. Rep.*, 2015, **5**, 13801.

80 J. Masa, P. Weide, D. Peeters, I. Sinev, W. Xia, Z. Sun, C. Somsen, M. Muhler and W. Schuhmann, Amorphous Cobalt Boride (Co$_2$B) as a Highly Efficient Nonprecious Catalyst for Electrochemical Water Splitting: Oxygen and Hydrogen Evolution, *Adv. Energy Mater.*, 2016, **6**, 1502313, DOI: **10.1002/aenm.201502313**.